



Examining temporal and spatial variations of internal temperature in large-format laminated battery with embedded thermocouples



Zhe Li^a, Jianbo Zhang^{a,*}, Bin Wu^a, Jun Huang^a, Zhihua Nie^b, Ying Sun^b, Fuqiang An^b, Ningning Wu^b

^a State Key Laboratory of Automotive Safety and Energy, Tsinghua University, Beijing 100084, China

^b Citic Guoan Mengguli Power Source Technology Co., Ltd, Beijing 102200, China

HIGHLIGHTS

- Thermocouples embedded inside a cell detected significant temperature variation.
- Internal temperature differed appreciably from the surface for thin laminated cell.
- Center layer thermal response time was 485–620 s, 27–70 s larger than the surface.
- In-plane temperature variation was much larger than through-plane direction.
- Forced convection was effective in suppressing temperature rise and variation.

ARTICLE INFO

Article history:

Received 12 January 2013

Received in revised form

16 March 2013

Accepted 23 April 2013

Available online 30 April 2013

Keywords:

Lithium-ion battery

Embedded-thermocouples

Internal temperature measurement

Temperature variation

Hot spots/zone

Time constant of thermal response

ABSTRACT

Information on battery internal temperature is valuable to enhance the understanding of thermo-electrochemical reactions, to validate simulation models, and to refine battery thermal design. In this study, 12 thermocouples are embedded at strategically-chosen locations inside a 25 Ah laminated lithium-ion battery. Another 12 thermocouples are attached at the corresponding locations on the surface. The temporal and spatial variations of the temperature are measured at a series of discharge rates under different thermal conditions. The thermal response of these locations is also analyzed. The major findings include: First, the internal temperatures could differ from the surface for as large as 1.1 °C, even for a thin laminated cell. Second, the time constants of thermal response at the internal locations are generally dozens of seconds larger than on the surface. Third, the internal variation in the plane direction reaches above 10 °C under adiabatic 1.5 C discharge, much larger than in the through-plane direction, indicating the in-plane heat conductivity needs improvement. Finally, forced convection is effective to suppress the temperature rise as well as the variation. The direct measurement of internal temperature initiated in this study paves the way for implanting sensors/microchips in single cell to extract multiple physico-electrochemical signals simultaneously.

© 2013 Elsevier B.V. All rights reserved.

1. Introduction

Battery temperature is measured for experimental research or monitored for the management of BTMS (battery thermal management system) of electric vehicles. The measurement methods of battery temperature could be classified into three types according to the location of temperature sensors.

- (1) First, temperature sensors are located outside individual cell. Generally, for battery packs of commercialized electric vehicles, most of the existing methods use the one-point temperature

on the cell surface to represent the overall state of the cell (2010 Toyota Prius) [1–4]. Besides cell temperature monitoring, with other sensors located in the cooling system (GM Volt) or on top of the sub-modules (Tesla Roadster), the multi-point temperature distribution of the battery pack is obtained.

- (2) Second, single temperature sensor has been reported mounted on top of the cell and sealed inside [5], but neither of them is located between the electrodes. Therefore, it's difficult to determine whether the internal temperature is monitored. Meanwhile, with the single location of temperature sensor, it's impossible to measure the temperature distribution inside the cell.

The above two types of measurement methods adopt the temperature at single location out of the electrodes to evaluate cell

* Corresponding author. Tel.: +86 10 62786918.

E-mail address: jbzhang@mail.tsinghua.edu.cn (J. Zhang).

thermal conditions. For small cells used in electronic products like cell phones and laptops, the associated error may be negligible. However, for large-format traction battery, the temperature variation at different locations inside the battery develops, and the temperature at one point on the surface can no longer represent the overall state. Under severe nonuniform temperature distribution, local hot spots may form, impairing cell durability or even triggering safety problems.

(3) Third, the sensors are inserted deeply into the cell to obtain internal temperature.

The information of battery internal temperature is valuable to reveal the location of internal hot spots/zones, to elucidate the mechanism of heat accumulation, and to refine the thermal design of the cells in aspects like the structure (cylindrical, prismatic or laminated), the cell capacity, and the configuration of the key components like the tabs. Besides helping to improve cell design, the information of internal temperature is also needed to achieve a sufficient validation of existing thermo-electrochemical simulation models. The existing battery models are already rather sophisticated and are capable of describing the voltage/current/temperature/ Li^+ ion concentration in each individual electrode layer [6–8]. However, only the surface temperature, usually at one location is used to validate these models. The scarcity of internal information hinders the integrality of the model validation, leaving its accuracy and predicting capability questionable.

Notwithstanding the importance of the internal temperature, the trials to obtain the information are rarely found in the literature, probably due to the difficulty involved in introducing sensors into a single cell.

Christophe Forgez [9] designed a plug-in measurement method to detect the internal temperature of a cylindrical 26650 lithium iron phosphate battery. A T type thermocouple was inserted into the hole drilled on the top of the cylinder to measure the internal temperature of the battery. Several measures were taken to enhance the safety of the operation. First, the whole process was carried out in the argon glove box to ensure an inert environment; Second, the battery was nearly fully discharged before the drilling. Moreover, the hole was sealed with resin after the thermocouple was inserted.

Chi-Yuan Lee [10] fabricated a flexible micro temperature sensor by depositing the erosion-resistant parylene and other sensor material layer-by-layer using physical vapor deposition (PVD) technique. Two of these sensors were inserted into a spirally-wound prismatic lithium-ion battery to measure the internal temperature. Then, micro electro-mechanical systems (MEMS) were utilized to develop integrated micro temperature and voltage sensors on the same piece of stainless steel foil, and six micro sensors were embedded in the flow field of a high-temperature fuel cell stack to monitor local temperature and voltage in situ [11].

In this study, instead of being inserted into the battery afterward, multiple thermocouples were embedded between the layers of electrodes of a laminated cell during the manufacturing process. It had the following advantages: First, the sensors with reliable insulation were embedded during the manufacturing process to avoid piercing the internal structure and triggering internal short; Second, the vacuum degree and the atmosphere inside the battery were kept essentially unchanged from an ordinary cell, therefore the battery was more reliable and might achieve longer cycle life before the failure; Third, multiple sensors could be readily accommodated and the location of each sensor could be precisely controlled, which was critical to quantitatively distinguish the temperature of different locations. Using the thermocouple-embedded cell, the temporal and spatial variations of the temperature were measured during

Table 1
The specification of the two cells.

Cell specification	Value	
	Cell 1	Cell 2
Capacity (1/3 C)	5 Ah	25 Ah
Nominal voltage	3.8 V	
Nominal resistance (1 kHz)	5 m Ω	1 m Ω
EODV (end of discharge voltage)	3 V	
Recommended charging method	CC–CV	
EOCV (end of charge voltage)	4.2 V	

constant-current discharge at a series of C-rates and different thermal boundary conditions.

To the author's knowledge, this study initiated the direct measurement of the internal temperature at multiple locations inside large-format laminated traction battery. The measured temperature variation under different thermal boundary conditions revealed the thermal property of the tested cell, identified the direction for the improvement of cell thermal design and the ways for effective thermal management. The measured results are currently being used to validate our thermo-electrochemical model. Moreover, it has explored the feasibility of implanting sensors into a single cell, which was previously considered fragile and zero-tolerant of intruders. This attempt paves the way for the research of smart cell, a cell that can monitor and manage itself, with sensors sandwiched between the electrode layers and microchips sealed inside.

2. Specifications of the tested cells and locations of the embedded thermocouples

The constant-current discharge experiments under a series of C-rate in different thermal boundary conditions were carried out on two types of sensor-embedded LiMn_2O_4 /graphite laminated cells, 5 Ah and 25 Ah. The specifications of the two cells are shown in Table 1.

Fig. 1 shows the EIS (electrochemical impedance spectroscopy) results of the sensor-embedded 25 Ah cell and another ordinary (without embedded sensor) 25 Ah cell. It was concluded that the EIS result of the sensor-embedded 25 Ah cell was quite similar with ordinary cell. The cell consistency was proved to be satisfactory, and the thermal behavior of the sensor-embedded 25 Ah cell should be representative of this cell model.

The specifications of the sensors embedded inside the cells are shown in Table 2.

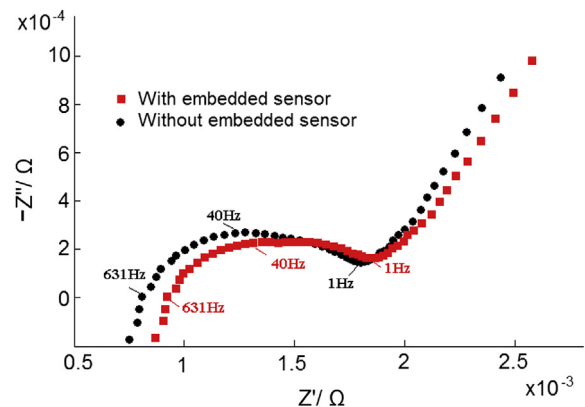


Fig. 1. The EIS results of the two 25 Ah cells with and without embedded sensors.

Table 2
The specification of the temperature sensors.

Specification	Value
Type	Type T thermocouple
Insulation material	Fiberglass
Diameter without insulation	0.125 mm
Diameter with insulation	<0.5 mm
Batch divergence	0.3 °C
Time constant	35 ms

Fig. 2 illustrates the locations of these embedded thermocouples. For the 5 Ah cell, thermocouples S1, S2, S4, and S5 were affixed to each corner of a piece of its separator by heat-resistant tapes while thermocouple S3 was affixed in the center. For the 25 Ah cell, thermocouples were cautiously affixed on special locations of a piece of its separator: (1) A8 in the center; (2) A7 and A9 on the vertical symmetry axis of each tab (L1 and L3), as well as on the horizontal symmetry axis of the cell (L4); (3) A5 and A11 on the same circumference with A7 and A9, as well as on the vertical symmetry axis of the cell (L2); (4) A4 and A6 on L1 and L3, as well as aligned with A5; (5) A1 and A3 on L1 and L3, and 20 mm to the top of the electrode plate; (6) A10 and A12 on L1 and L3, and 20 mm to the bottom of the electrode plate; (7) A2 in the middle of A1 and A3. All the internal thermocouples were then covered by another piece of separator. In addition, thermocouples B1–B12 were affixed on one side of the 25 Ah cell surface, at the corresponding locations as A1–A12.

The internal thermocouples sandwiched by two pieces of separators were then placed in the middle of the thickness, with the positive and negative electrode plate covering each side. The cells were then vacuumed and sealed, with extra glue on the entrance of the thermocouple lead wires against leakage.

The techniques to place and to protect the internal thermocouples should be highlighted to ensure the safety of the cells and the accuracy of the measurement: (1) The diameter of the thermocouples was chosen at the same level as the thickness of a pair of

electrodes, i.e. hundreds of micrometers, to prevent severe deformation of the laminated layers and decrease the damage to adjacent active material; (2) Mechanically reliable thermocouples were chosen to prevent breakage during the vacuum pumping and the assembling process; (3) The thermocouples were insulated properly to prevent internal short; (4) The entrance of each thermocouple was sealed reliably to prevent air/moisture to get into the cell, which was essential to keep the inside vacuum degree and the atmosphere unchanged from an ordinary cell; (5) The location of each thermocouple was strictly pinpointed with heat-resistant tapes.

Fig. 3(a) and (b) is the completed cells of 5 Ah and 25 Ah with the embedded sensors.

3. Experiments and results

The constant-current discharge experiments under a series of discharge rates were carried out on the sensor-embedded 25 Ah cell in different ambient conditions, as shown in Table 3.

An adiabatic calorimeter was adopted in the adiabatic tests no. 1.1–1.4. The cell was placed in the middle of the cavity, sitting over a beaker to avoid direct contact with the wall. Table 4 shows the detailed specification of this calorimeter.

During the natural convection tests, the cell was placed in a room without ventilation, still with the beaker below to expose the maximum surface area in the air.

During the forced convection tests, the cell was placed in an environment chamber, which was equipped with the heater and refrigeration compressor, and generated strong forced convection inside the box to realize constant temperature. Table 5 shows the detailed specification of this environment chamber.

It should be noticed that whether the tabs are wrapped or bare in the environment has significant impact on battery temperature distribution, especially in a well-ventilated environment. In this study, the tabs were wrapped with insulating tapes in all tests, firstly to guarantee the insulation to the cavity of the calorimeter and the environment chamber. Moreover, for the real battery

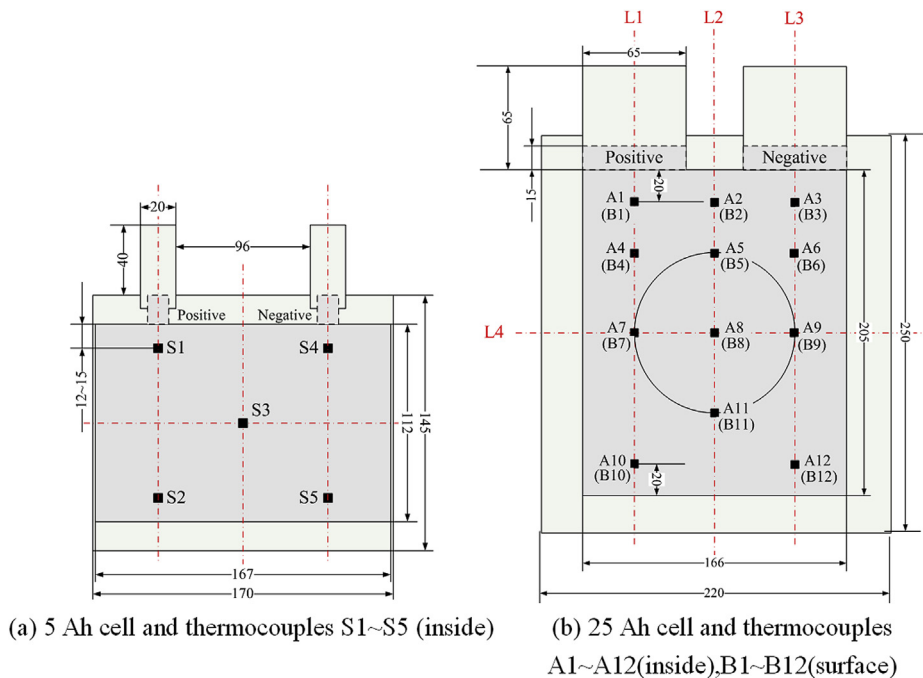


Fig. 2. The dimensions of the cells (unit: mm) and the locations of the thermocouples.

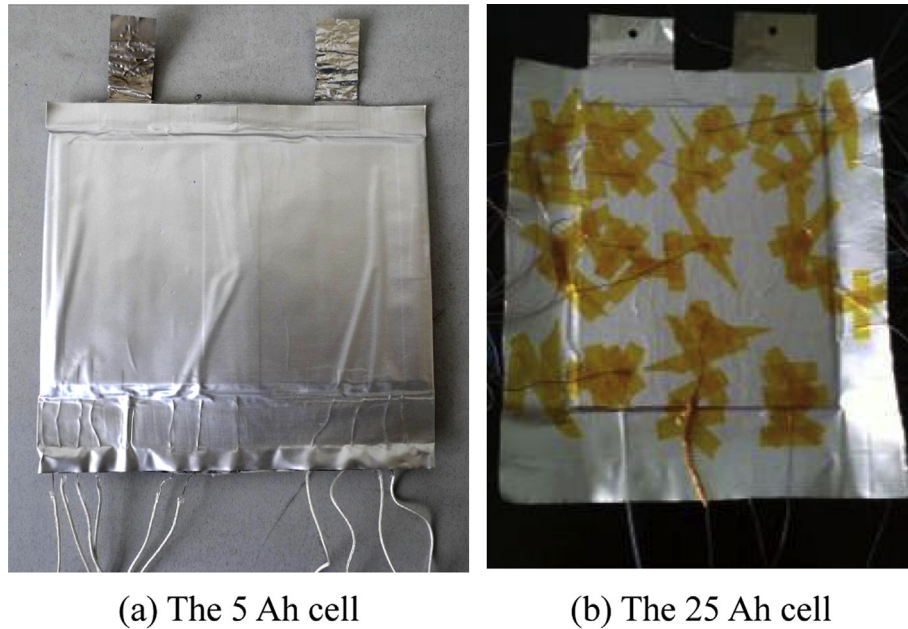


Fig. 3. The sensor-embedded cells.

Table 3

Test no., ambient conditions and discharge rates.

Test no.	Ambient condition	Discharge rate
1.1	Adiabatic condition	0.3 C
1.2		0.5 C
1.3		1 C
1.4		1.5 C
2.1	Natural convection	0.3 C
2.2		0.5 C
2.3		1 C
2.4		1.5 C
3.1	Forced convection	0.3 C
3.2		0.5 C
3.3		1 C
3.4		1.5 C

system on electric vehicles, the tabs are certainly not exposed in the space for safety concerns. Therefore, it is believed that the experimental data obtained from the sensor-embedded cell with wrapped tabs is more representative of its real thermal property when used in battery system of electric vehicles.

The voltage/current of the cell and the temperature of all the thermocouples were measured and recorded during the tests.

3.1. Discharge voltage curves

Due to the large number of tests, only the discharge voltage curves of four different discharge rates under forced convection are shown. Fig. 4 compares the discharge curves of two 25 Ah cells with and without embedded sensors. The cell capacity had not been greatly affected by the embedded sensor.

Table 4

The specification of the adiabatic calorimeter.

Specification	Value
Manufacturer	HEL (U.K.)
Type	PHITEC1&BTC (combination)
Sensitivity	0.005 °C min ⁻¹

Table 5

The specification of the environment chamber.

Specification	Value
Manufacturer	HENGDA (P.R.C.)
Type	SDH0005
Range	0 °C–100 °C
Accuracy	2 °C

3.2. Temperature curves

Due to the large number of tests, instead of listing all temperature curves, only some representative ones are shown in Fig. 5–7.

Part of the temperature curves increased monotonically with the ongoing of discharge process, such as the 1.5 C discharge under the adiabatic condition (Test no. 1.4). Fig. 5 shows the temperature changes of 12 locations inside the cell (a) and the other 12 locations on the surface (b).

However, some of the temperature curves were not monotonically increasing during the entire discharge process, e.g., the

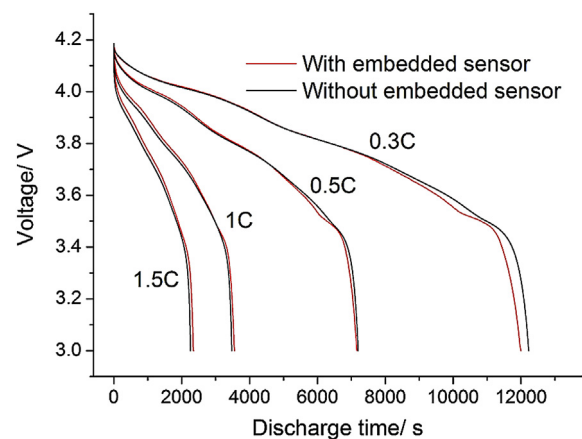


Fig. 4. Discharge curves of two 25 Ah cells with and without embedded sensors under the forced convection.

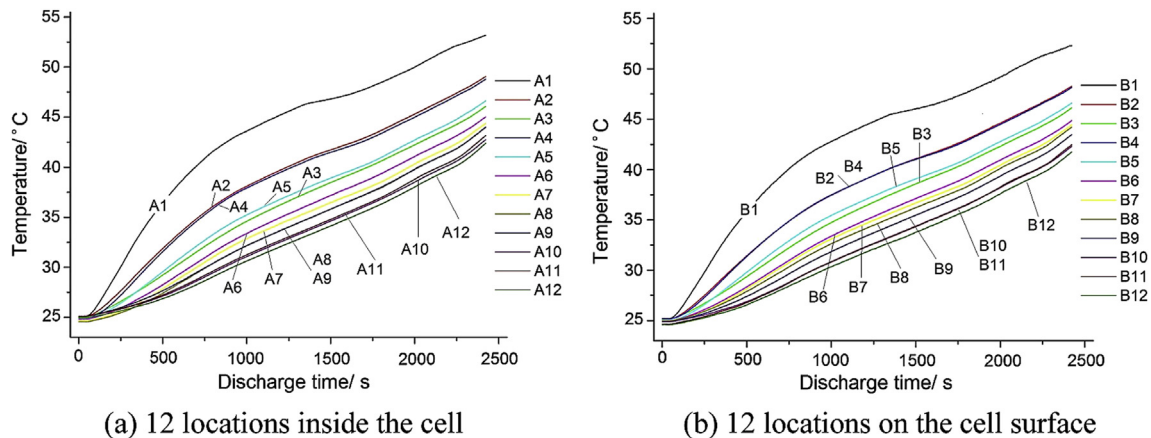


Fig. 5. Temperature changes when discharged at 1.5 C under the adiabatic condition (Test no. 1.4).

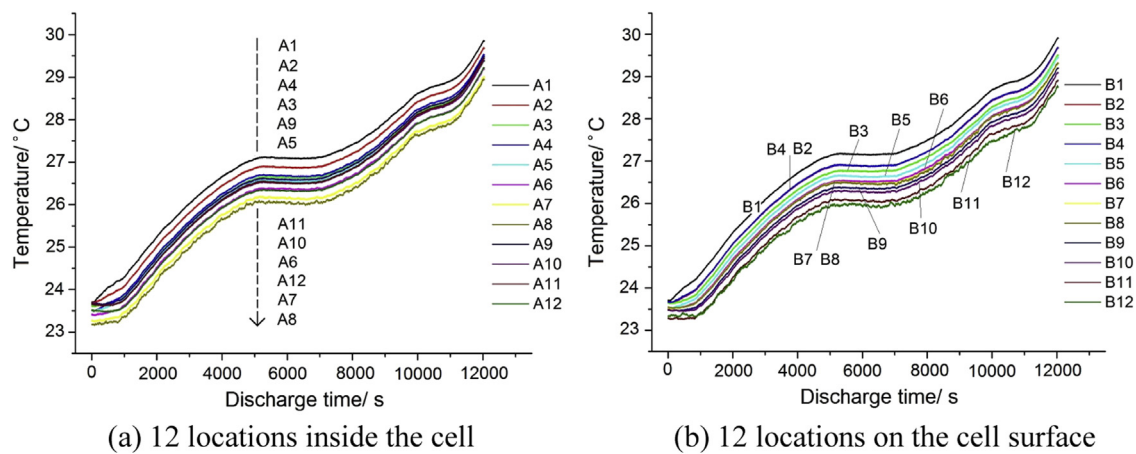


Fig. 6. Temperature changes when discharged at 0.3 C under the adiabatic condition (Test no. 1.1).

temperature curve of 0.3 C discharge under the adiabatic condition (Test no. 1.1) had a plateau in the middle, as shown in Fig. 6(a). Another example is 0.3 C and 0.5 C discharge under natural convection (Test no. 2.1 and 2.2): The temperature curves showed strong fluctuations, wherein the highest temperature of the 0.3 C curve (Test no. 2.1) did not appear in the end of discharge, but in the DOD (depth of discharge) of 30%–40%, as shown in Fig. 7. The

temperature curves of 0.3 C, 0.5 C, 1 C under forced convection (Test no. 3.1, 3.2 and 3.3) also fluctuated during the discharge.

In summary, with the existence of convective heat transfer, since the heat dissipation rate was related to the temperature difference between the battery and environment, the instantaneous heat dissipation rate kept changing when the battery temperature varied, which resulted in a dynamic equilibrium between the heat

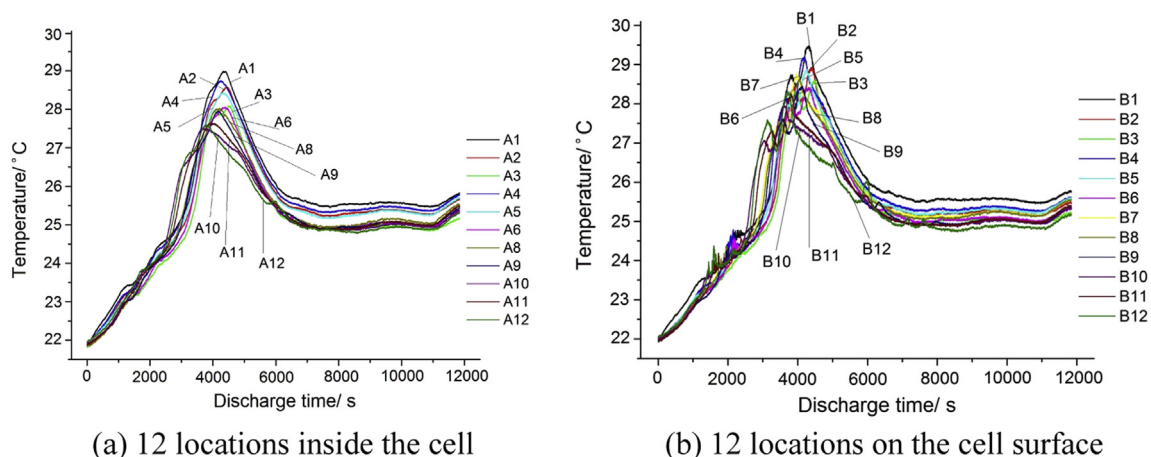


Fig. 7. Temperature changes when discharged at 0.3 C under the natural convection condition (Test no. 2.1).

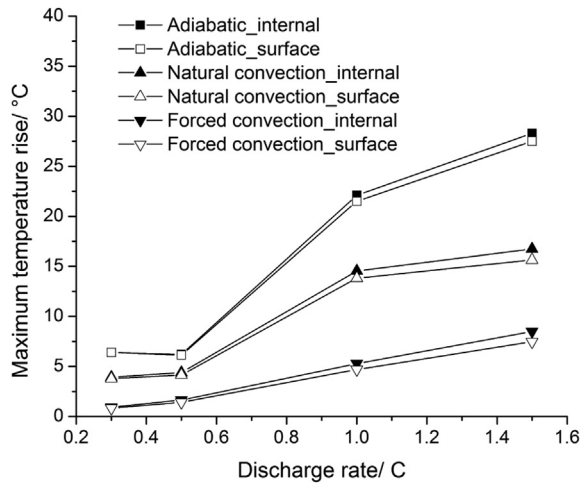


Fig. 8. The maximum temperature rise of the 25 Ah cell (inside and surface) at the end of discharge (0.3 C, 0.5 C, 1 C, 1.5 C) under three different boundary conditions Note: For the 0.3 C discharge test under natural convection, Fig. 8 does not reflect the maximum temperature rise of the entire discharge process (occurred at 30%–40% DOD), but only the temperature rise at the end of discharge.

Table 6

The maximum rise of the internal and surface temperature at the end of 1 C discharge under the adiabatic condition (5 Ah and 25 Ah cells).

Capacity (Ah)	Position	Maximum temperature rise at the end	
		Value (°C)	Location of the hottest spot
5	Inside	7.3	Near the positive tab (measured by embedded thermocouple S1)
	Surface	7.0	Near the positive tab (measured by infrared thermal imaging)
25	Inside	22.1	A1
	Surface	21.5	B1

dissipation and generation rate, and caused the fluctuation of the temperature curves.

4. Discussion and analysis

Discussions in Section 4.1 and 4.2 mostly focus on temporal variations, whereas Section 4.3 and 4.5 are mainly about the discussions on spatial variations.

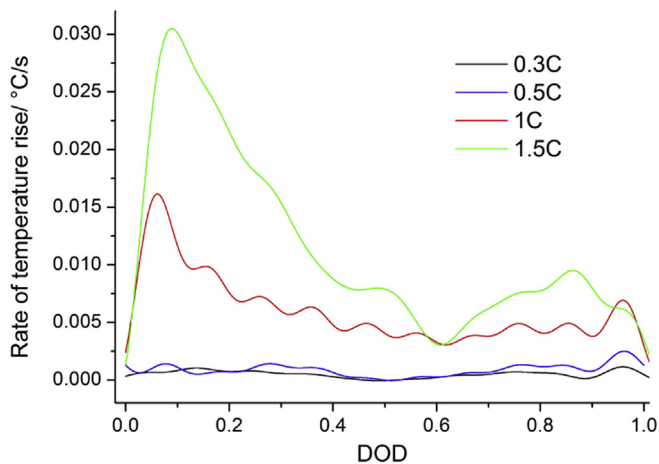


Fig. 9. The rate of temperature rise of A1 under the adiabatic condition.

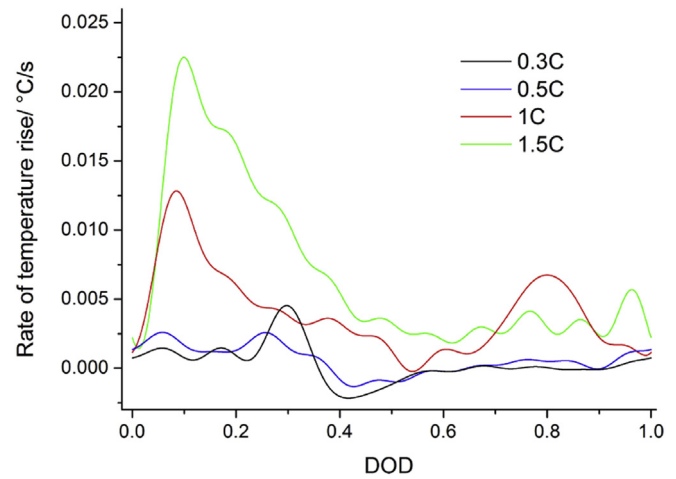


Fig. 10. The rate of temperature rise of A1 under the natural convection condition.

4.1. The maximum temperature rise

The maximum temperature rise of the hottest spot inside the cell has always been listed in the top concerns when analyzing the thermal characteristics of traction battery since it could trigger permanent battery capacity fade and even extremely dangerous thermal runaway.

With the accumulation of working cycles, the active material near the hottest spot has suffered from hot temperature and the capacity degradation of the cell may firstly take place from the hottest spot. Therefore, reducing the temperature of the hottest spot is one of the main tasks in improving the cell thermal design. For durability concerns, a well-ventilated local environment should be preferentially offered to the potential hottest locations in BTMS.

When a cell is abusively used and heated up to a marginal high temperature by severe discharge profiles, some exothermic side reactions may happen to the electrolyte and the active material near the hottest spot, and the local separator layers may shut down or collapse ahead of other locations. In this case, the delicate balance of the heat generation and transfer at the hottest location is critical to prevent battery thermal runaway and protect the safety of the power system. Fig. 8 shows the maximum temperature rise among all the temperature data from the thermocouples at the end of discharge under three different boundary conditions.

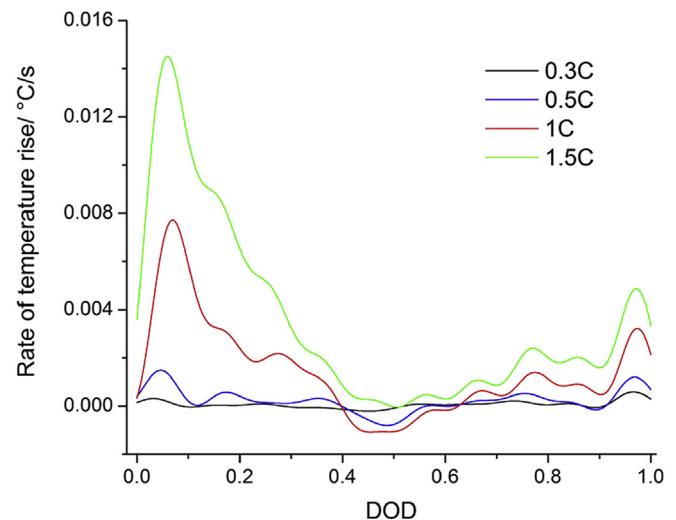


Fig. 11. The rate of temperature rise of A1 under the forced convection condition.

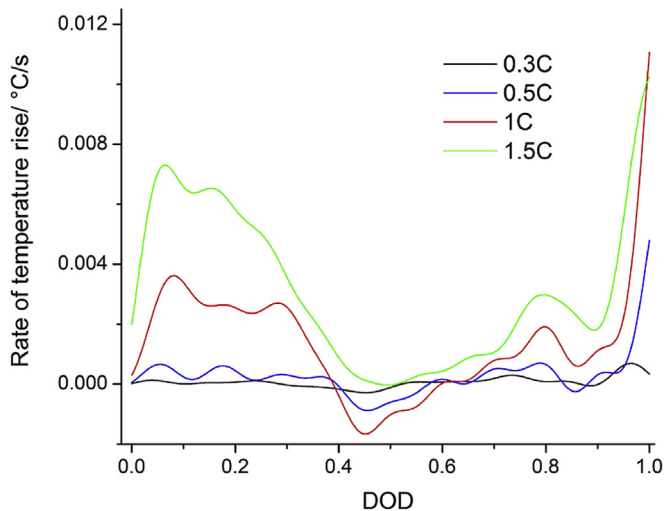


Fig. 12. The rate of temperature rise of A5 under the forced convection condition.

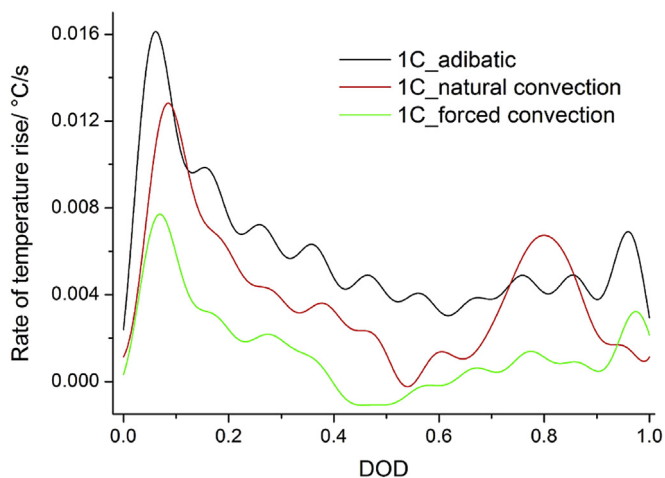


Fig. 13. The rates of temperature rise under three different boundary conditions (discharge rate 1 C).

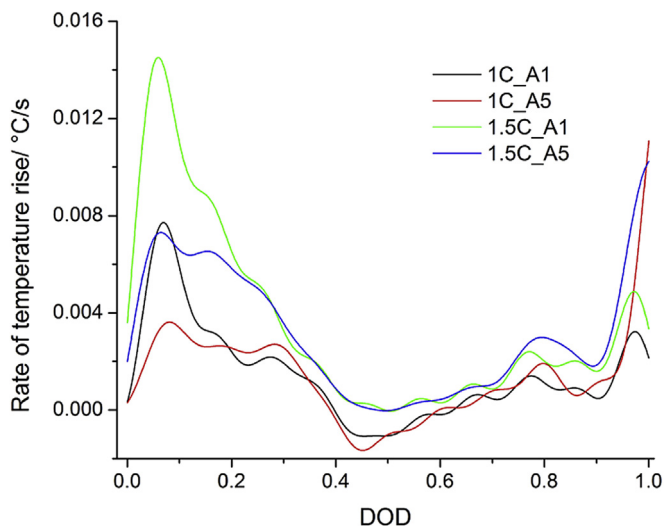


Fig. 14. The rates of temperature rise of A1 and A5 under the forced convection condition (discharge rate 1 C and 1.5 C).

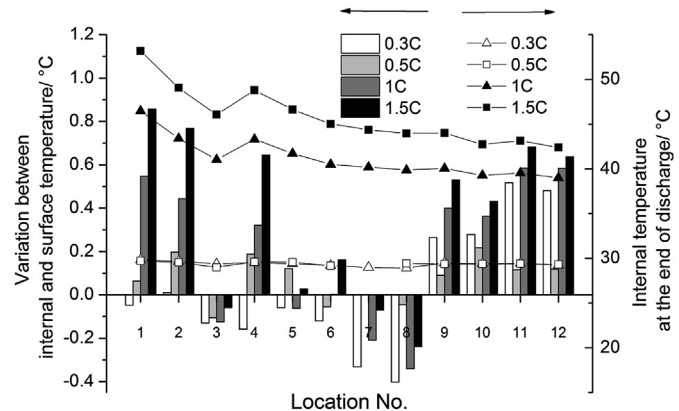


Fig. 15. The temperature variation of internal and surface locations under the adiabatic condition. Note: Some data of location no. 7 was missing because the internal thermocouple A7 failed during the tests. The same hereinafter.

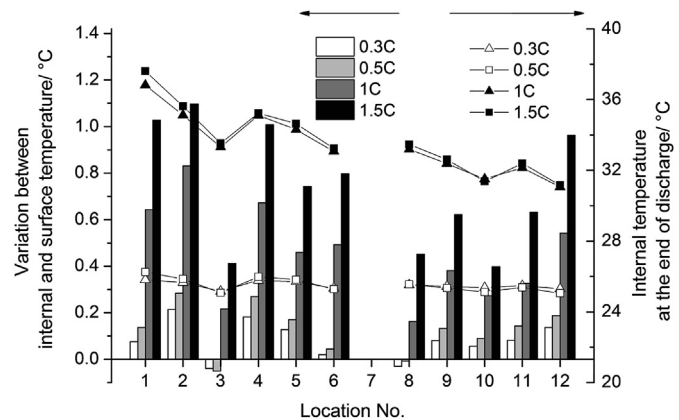


Fig. 16. The temperature variation of internal and surface locations under the natural convection condition.

(1) The correlation between the maximum temperature rise and discharge rates

The maximum temperature rise increased monotonically with the discharge rates, and the relationship could be approximated as linear in the range of 0.3 C–1.5 C.

(2) The correlation between the maximum temperature rise and boundary conditions

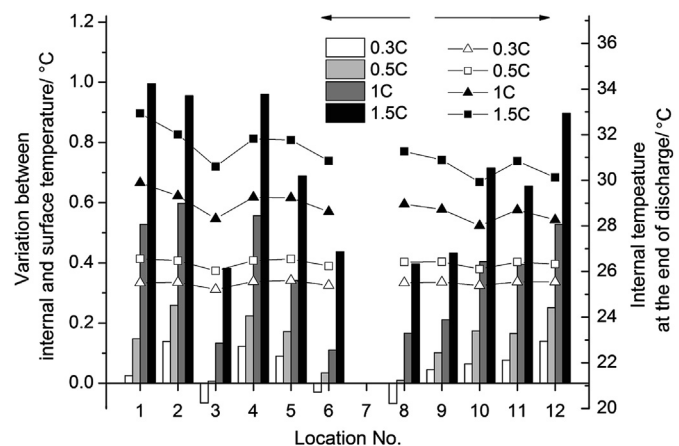


Fig. 17. The temperature variation of internal and surface locations under the forced convection condition.

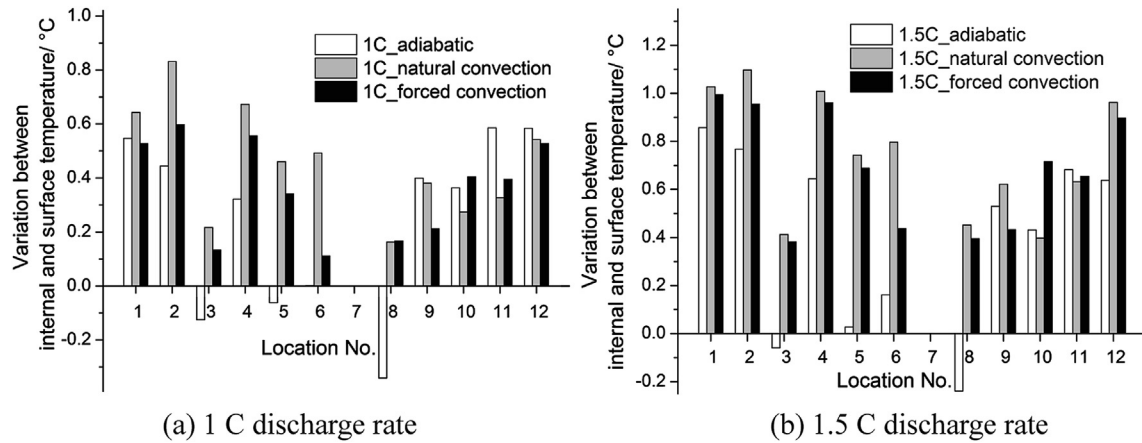


Fig. 18. The temperature difference of inside and surface under three different boundary conditions.

The maximum temperature rise kept decreasing when the boundary conditions were changed from adiabatic to natural convection, and then forced convection. Establishing appropriate heat dissipation environment is helpful to control the thermal balance and suppress the temperature rise of the battery.

(3) The difference between internal and surface temperature rise

In general, the maximum temperature rise inside the cell was higher than on the surface. Meanwhile, the difference was getting higher with the increase of discharge rates. Detailed discussion on the difference between internal and surface temperature will be carried out in Section 4.3.

(4) The correlation between the maximum temperature rise and cell capacity

Comparison tests of 1 C discharge were carried out on the 5 Ah thermocouple-embedded cell under the adiabatic condition. The maximum rise of internal and surface temperature of the 5 Ah cell was compared with 25 Ah cell in Table 6, and the temperature rise shows strong sensitivity to the cell capacity given the same discharge rate and boundary condition.

4.2. The rate of temperature rise

The rate of temperature rise (unit: $^{\circ}\text{C s}^{-1}$) for the hottest spot (such as A1 or A5) was drawn in Figs. 9–12, with the horizontal axis normalized to DOD. All the rate curves have been refined by 10 Hz low-pass FFT filter. The change of rate with DOD, as well as its relationship with the discharge rates and boundary conditions, was observed.

(1) The curve shape of temperature rise rate with DOD

For all the rate curves in Fig. 9–12, the rate in the beginning of discharge increased rapidly to reach the peak in a short period of time (0%–20% DOD), and then gently declined to a relatively stable value. At the later part of discharge (80%–100% DOD), the rate of temperature rise appeared to grow again. This second growth was the clearest in the forced convection condition, wherein the rate curve of A5 exhibited more activity than A1.

(2) The correlation between the rate of temperature rise and discharge rates

In general, the instantaneous rate of temperature rise was higher at larger discharge rate. Under the adiabatic condition, the peak rate of temperature rise of 1.5 C was six times higher than 0.5 C (Fig. 9).

(3) The impact of boundary conditions on the rate of temperature rise

Fig. 13 shows the rates of temperature rise when discharged at 1 C under three different boundary conditions. The instantaneous rate was decreasing with the improving of ventilation.

(4) Different rate curves of A1 and A5 under the forced convection

Fig. 14 shows the rates of temperature rise of A1 and A5 under the forced convection. At the same discharge rate, in the beginning part of the curve, the peak rate of A1 was significantly higher than A5. However, the A5 curve demonstrated a much stronger ‘second growth’ after 90% DOD than A1, and it even surpassed the initial peak and reached the maximum rate at the end.

4.3. The temperature variation of internal and surface locations

4.3.1. The temperature variation at the end of discharge

The multiple embedded-thermocouples inside the cell revealed to us the real difference between the internal and surface temperature for the first time. Columns in Figs. 15–17 show the

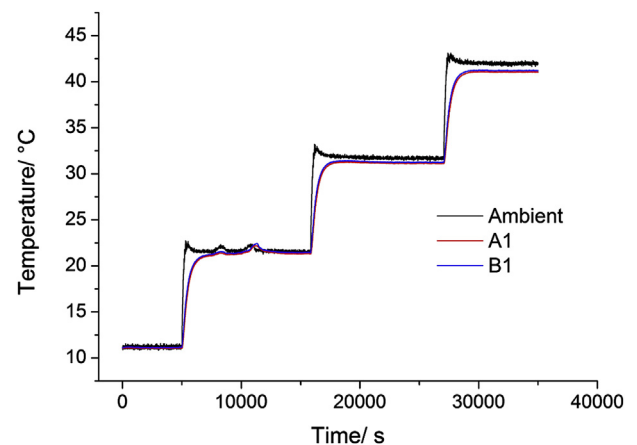
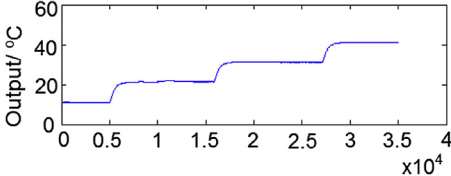
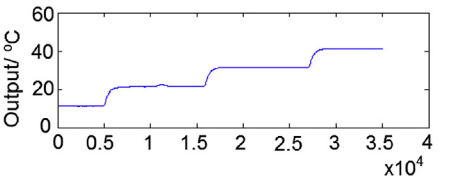
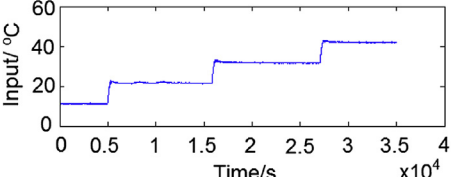
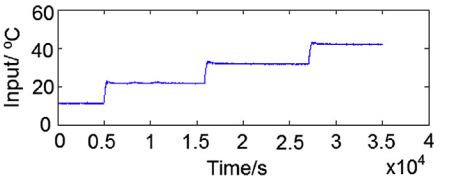
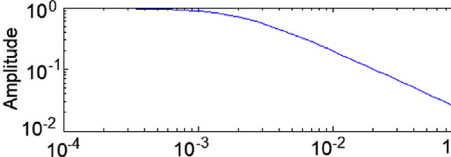
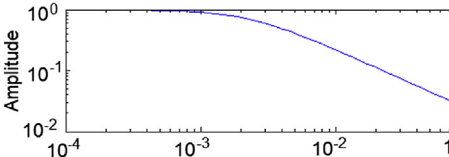
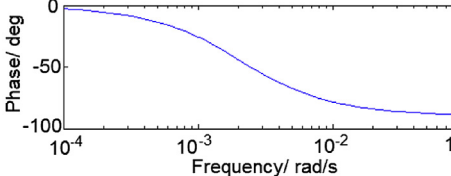
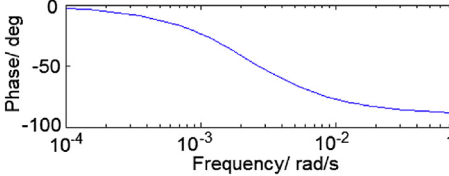
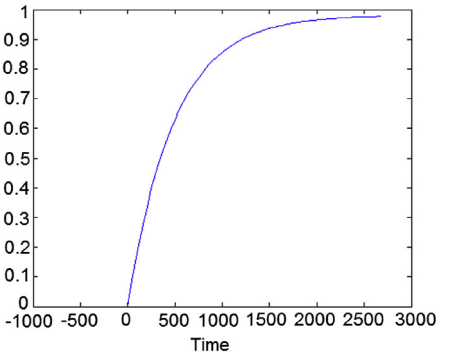
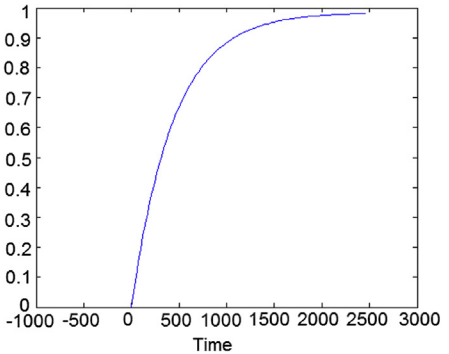
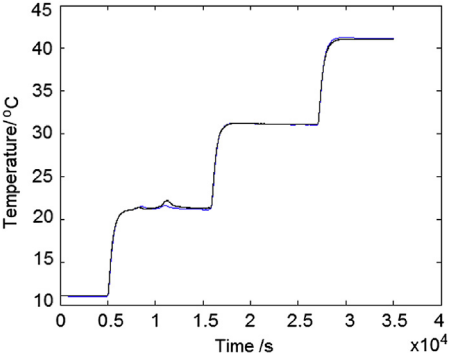
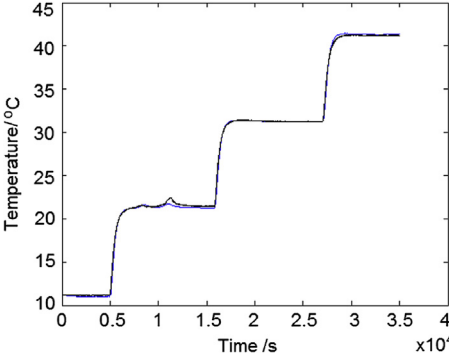


Fig. 19. The temperature of ambient environment, A1 and B1.

Table 7
The transient temperature response characteristics of A1 and B1 while heated up from outside (full temperature range of Fig. 18).

	A1 (Inside)	B1 (surface)
Time constant τ	485 s	439 s
Input and output curves		
		
Frequency response characteristics		
		
The unit step response characteristics		
Comparison between model identification and experimental results		

temperature difference between the internal locations A1–A12 and their corresponding locations B1–B12 on the surface under four discharge rates and three types of boundary conditions, while the dots-and-lines in these figures show the internal temperature of these locations at the end of discharge.

- (1) From the comparison at each location number, the internal temperature was generally larger than the surface, and the maximum difference could be as large as 1.1°C even for the thin laminated cell of 7 mm under a moderate discharge rate of 1.5 C. The surface temperature was insufficient to fully represent the overall thermal state of the cell. Therefore, in the thermal design of single cells or the management of battery packs, if the surface temperature is directly adopted to estimate the temperature extremes within the system, it could result in overestimation of system thermal safety and misjudgment of the effectiveness of cell design or pack management.

The questionable phenomenon that some internal temperatures in Fig. 15 were lower than surface is attributed to the limitation of the test equipments. First, the resolution of thermocouple is 0.3°C , and the negative column in Fig. 15 reached about -0.3°C . Therefore, it is difficult to conclude whether this ‘questionable phenomenon’ really exists or just due to the resolution insufficiency. It has practical difficulty to further improve the resolution due to the special insulation/anti-corrosion requirements for thermocouples embedded inside cell. Second, although the adiabatic calorimeter had been calibrated to suppress its deviation to a considerably small amount before the tests, in some cases, the adiabatic environment in the calorimeter could be slightly violated, and the cavity may actually heat up the cell instead. This deviation is attributed to the feedback control algorithm of the calorimeter: The adiabatic calorimeter keeps tracking the cell temperature through the feedback-control of the heaters in the chamber to achieve adiabatic environment. The feedback sensor of cell temperature is arranged at a single point on cell surface, which makes the feedback information spatially incomplete and triggers the occurrence of cavity-heating.

- (2) A positive correlation existed between the inside-and-surface temperature difference and the temperature level at this location. In Figs. 15–17, under each boundary condition, the rise and fall of the temperature difference columns coincided with the fluctuation of the temperature dots-and-lines, which represented the internal temperature at the end of discharge.

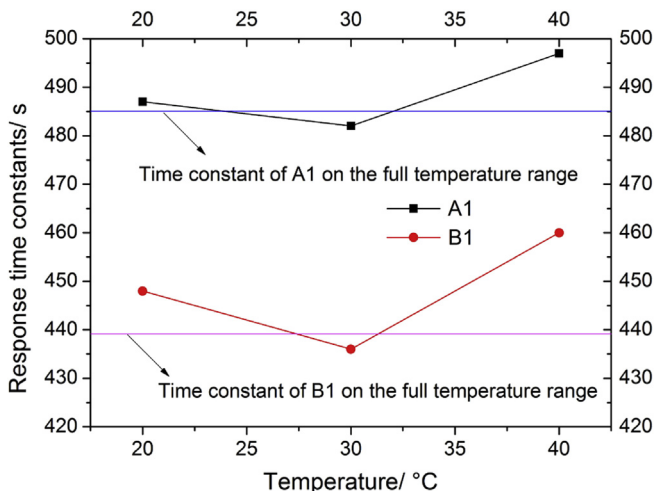


Fig. 20. The time constants of A1 and B1 within different temperature ranges.

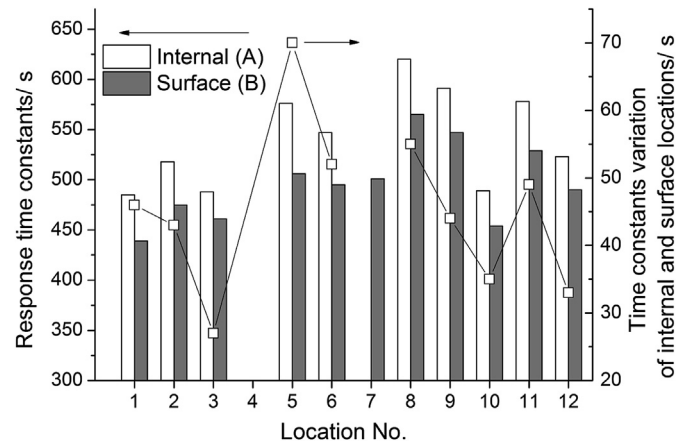


Fig. 21. The response time constants of different locations.

- (3) For natural and forced convection conditions, the inside-and-surface temperature difference was enlarged when the discharge rate increased. This correlation was not stringently observed for the adiabatic condition.
- (4) Sensitivity to boundary conditions

Compared with the adiabatic condition, the presence of natural convection aggravated the temperature difference of the inside and surface. However, the temperature difference then showed a trend of decrease when the convection was further enhanced, as shown in Fig. 18. Therefore, the ventilation environment for the battery pack in electric vehicles should be cautiously designed: The measured temperature on the cell surface may deviate from the internal temperature, especially when natural convection cooling is applied.

4.3.2. The response time variation during external heating

The temperature variation of internal and surface locations includes not only the temperature difference but also the different response characteristics to external heating. The comparative analysis was carried out below by identifying the different response time constants of internal and surface locations.

The 25 Ah cell was horizontally placed on the top of a beaker in the environment chamber and the initial temperature was set to 10°C in the beginning of an 8-h sufficient rest (only the last 1.5 h was sampled). Then temperature was consecutively adjusted to a sequence of 20°C , 30°C and 40°C , and kept for 3 h, 3 h and 2 h respectively. The sampling frequency was set to 1 Hz. Fig. 19 shows

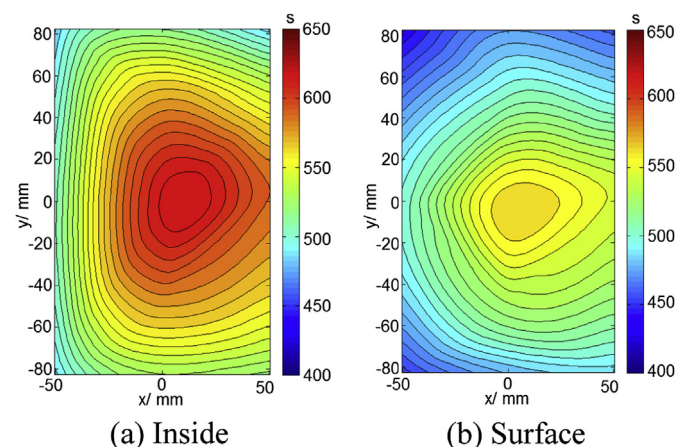


Fig. 22. The distribution of time constants.

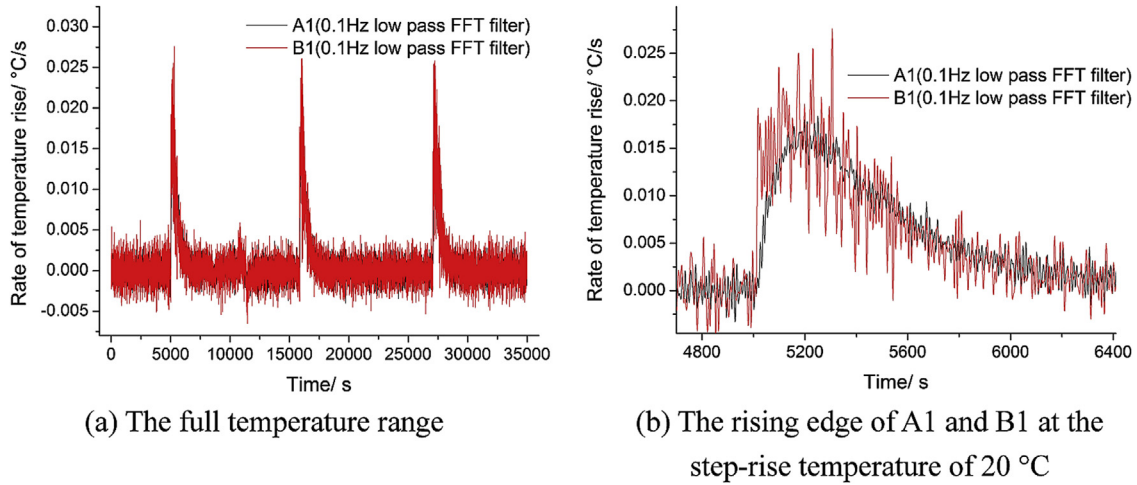


Fig. 23. The rate of temperature rise curves of A1 and B1.

the environment temperature inside the environment chamber, the temperature of thermocouples at A1 and B1.

The basic formula of battery thermal balance model is shown in Eqs. (1) and (2):

$$mC_p \frac{\partial T}{\partial t} = q_c + q_g \quad (1)$$

$$q_c = \nabla \cdot (k \nabla T) \quad (2)$$

In Eqs. (1) and (2):

m and C_p —the mass and the heat capacity of the target subject,
 T —the temperature of the target subject,
 q_c —sum of its heat conductivity rate of all dimensions,
 q_g —heat generation rate,
 k —heat conductivity coefficient.

The boundary condition of Eq. (2) is defined by the heat transfer of the target subject with the environment, as in Eq. (3).

$$k \nabla T \cdot \vec{n} = -h(T - T_a) \quad (3)$$

In Eq. (3)

h —convection heat transfer coefficient,

T_a —the ambient temperature,

\vec{n} —outward normal direction.

The target temperature T (output) and environment temperature T_a (input) can be correlated by the first-order differential equation drawn from the thermal models in Eq. (1)–(3). The system transfer function $G(s)$ of this first-order inertia process is as Eq. (4):

$$G(s) = \frac{1}{1 + \tau(\{T_a\})s} \quad (4)$$

$\tau(\{T_a\})$ implies that the time constant might be different when the input temperature profile $\{T_a\}$ changes.

The system identification toolbox in MATLAB was adopted to identify the response time constant $\tau(\{T_a\})$, and the input of the system was the ambient temperature in Fig. 19 while the outputs were the measured temperature of the internal and surface locations in the 25 Ah cell.

(1) The response characteristics of typical internal and surface spots

Identified from Fig. 19 (the input temperature profile covered the full temperature range), the transient temperature response

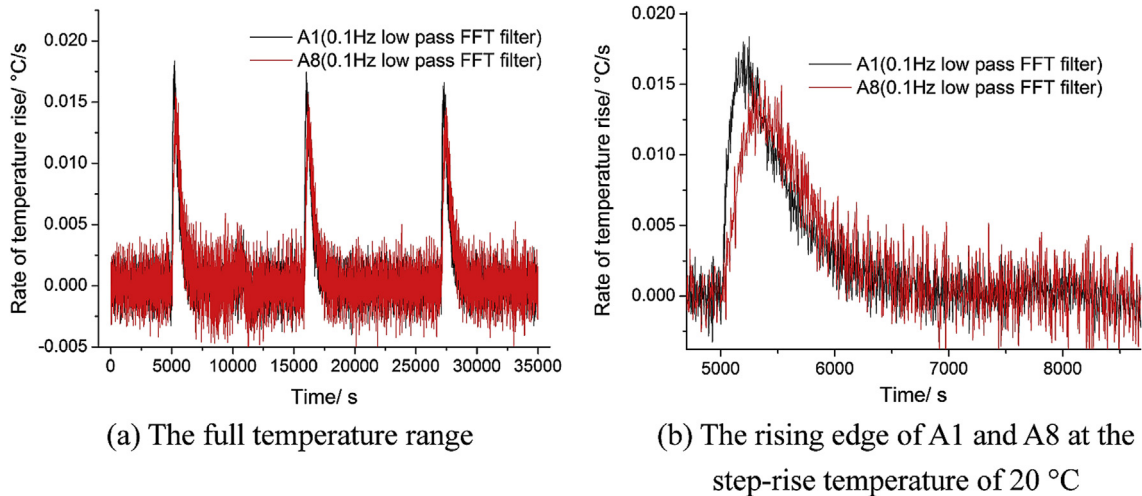


Fig. 24. The rate of temperature rise curves of A1 and A8.

characteristics of A1 and B1 were compared in Table 7. The time constant of A1 was 485 s, 10% larger than that of B1 (439 s).

(2) The response time constants within different temperature ranges

Fig. 20 compares the time constants of A1 and B1 within different temperature ranges, and the two horizontal lines represent the time constant identification results on the full temperature range in the external heating tests. It is shown that the time constants varied slightly in different ranges of step-rise temperature input.

(3) The response time constants at different locations

First, the time constants of 12 internal locations could differ greatly, and they were distributed from 485 s to 620 s, with the relative deviation of more than 20% (Fig. 21). The time constant was

closely related to the position: The maximum time constant appeared at the center point A8, and the second largest time constants occurred at the 4 points on the circumference, A5, A7, A9, and A11. It could be concluded that the locations in peripheral regions (near the cell corners) were more sensitive to external heating and would response faster on the temperature rise, as the contour lines shown in Fig. 22.

Second, the time constants of internal locations were generally larger than the spots on the surface, and the difference was distributed in the range of 27 s–70 s within 12 locations (Fig. 21).

(4) Error analysis

The identification error has been categorized into three parts according to the sources.

First, error from the response time of thermocouple: Since the time constant of the thermocouples (35 ms) is much shorter (10^{-4})

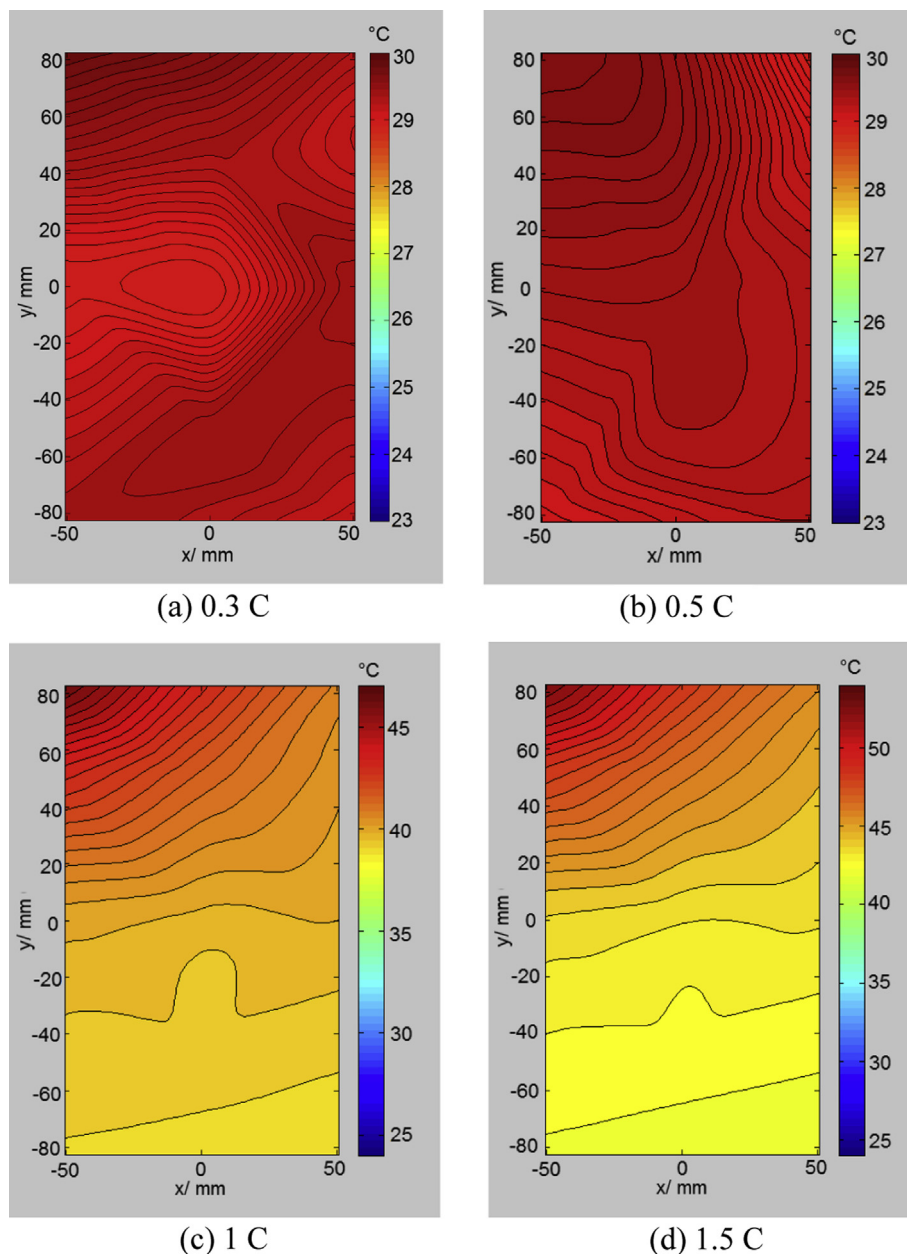


Fig. 25. The internal temperature distribution at the appearance of maximum temperature rise under the adiabatic condition.

than the cell time constants (in the range of 400–650 s), it can be neglected when discussing the cell thermal response.

Second, error from measurement uncertainty: The recognition results of time constant are affected by the accuracy of thermocouple readings. A numerical simulation has been carried out to find out the maximum deviation of time constant in the range of thermocouple divergence (0.3 °C). Taking spot A1 for example, a random number between [0, 0.3] was added to each of the temperature input and output values, and the time constant was re-identified. This simulation was repeated for ten times with different randomly-generated addend between [0, 0.3]. During all these numerical simulations, the maximum deviation of time constant is less than 3 s. Compared with the thermal time constant of spot A1 (485 s), or with the difference between A1 and B1 (46 s), the error from measurement uncertainty is minimum in the given range of thermocouple divergence.

Third, error from modeling and the algorithm used in parameter identification: This type of error could be evaluated in the Matlab system identification toolbox. Taking A1 for example, the tested and simulated temperature output array are assumed to be T_i^t and T_i^s ($i = 1, 2, \dots, n$, n is 34,990 in this case, relative to sample frequency). The variance (as in Eq. (5)) of this identification results is 0.2212, which proves the error from modeling and algorithm is acceptable.

$$V_{ar} = \frac{\sum_{i=1}^n (T_i^s - T_i^t)^2}{n} \quad (5)$$

(5) The transient rate of temperature rise

Besides the time constant analysis, the transient rate of temperature rise can also be used to describe the temperature

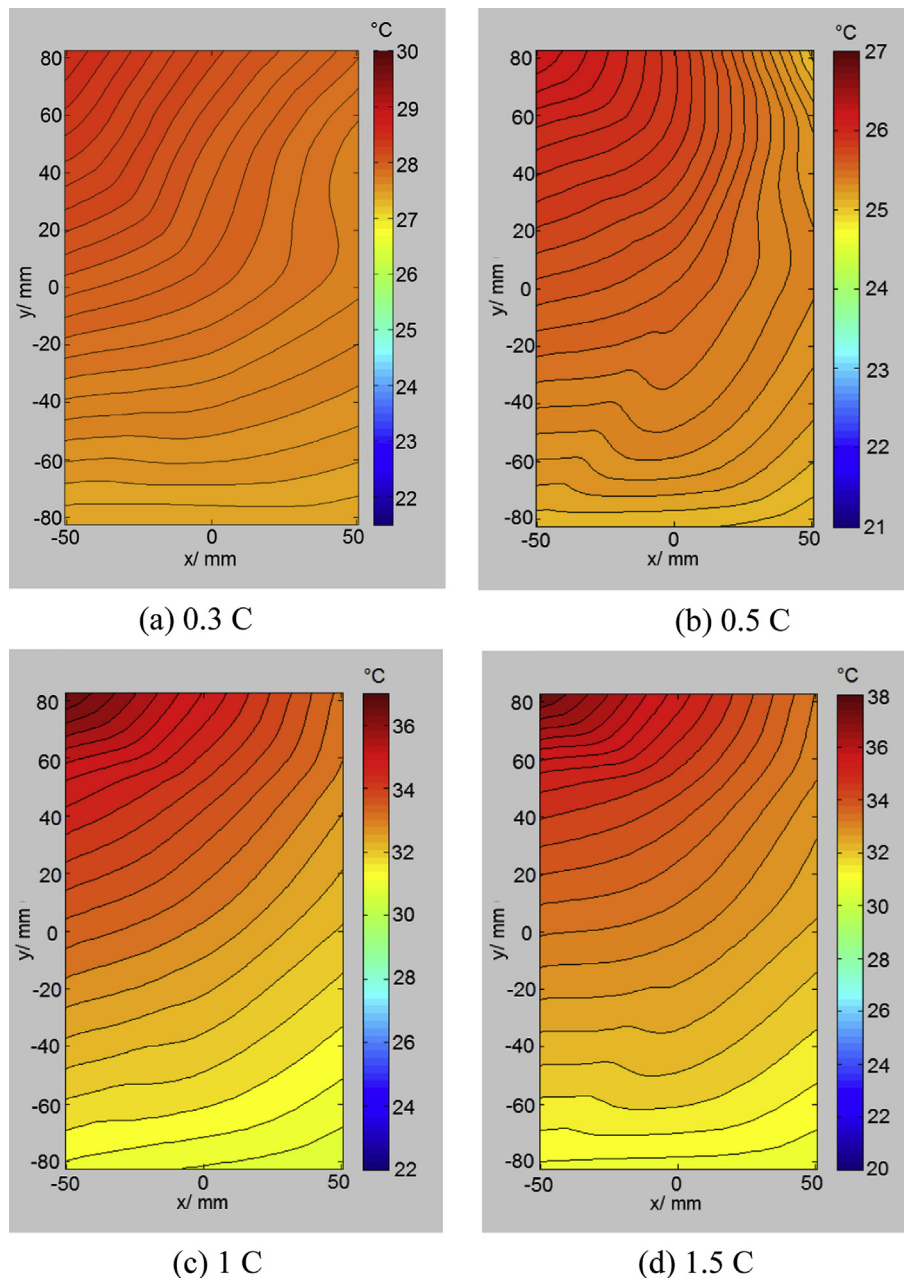


Fig. 26. The internal temperature distribution at the appearance of maximum temperature rise under the natural convection condition.

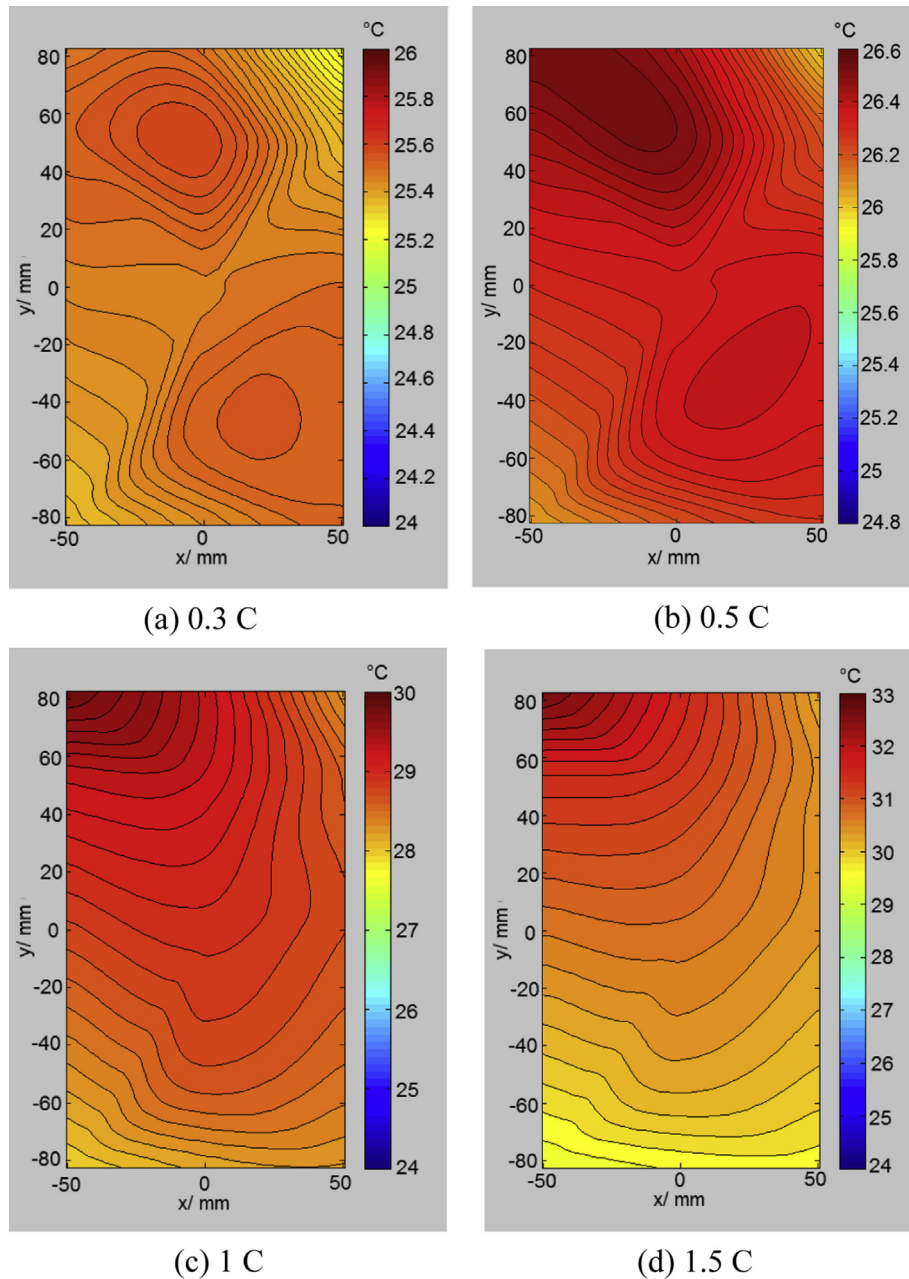


Fig. 27. The internal temperature distribution at the appearance of maximum temperature rise under the forced convection condition. Note: Due to the wide temperature range of all figures, the scales of all plots in Figs. 25–27 were chosen independently to show the distribution with high resolution. And the contour fields in Figs. 25–29 are plotted from the test data of the scattered 12 locations.

response characteristics during external heating tests. Generally, in the transient process, the rate climbed rapidly to reach the maximum, and then fell in a relatively slow speed to approximate zero.

First, the main difference of the rising rate between internal and surface locations appeared on the rising edge of the transient rate curves. In Fig. 23, the rising edge of B1 in the rate curve happened earlier and reached higher peak than A1, which explained the time constant variations of internal and surface locations.

Second, the rising edge of A1 in the rate curve happened earlier and reached higher peak than A8 (Fig. 24), which coincided with the strong temperature sensitivity of spots near cell corners to external heating.

Table 8

The DOD state when the location of the hottest spot shifted (5 Ah cell in adiabatic condition).

C-rate	Discharge capacity when the location shifted/Ah	DOD/(% (the total discharge capacity varied with C-rate))
1 C	No shift before the end of discharge	
2 C	4.14	92.76
3 C	4.25	96.84
4 C	4.35	99.56
5 C	4.22	99.29
6 C	No shift before the end of discharge	

4.4. The temperature distribution of 12 internal locations

(1) The position of the hot and cold zones

In general, as in Figs. 25–27, the hot zone located at the positive tab, the cold zone was at the bottom of the cell below the negative tab, and the temperature distribution gradient followed the line from the center of the hot zone to the cold zone. In other conditions, the hot zones appeared in double as round-shaped highlands in the contours, and located near the positive tab and lower right to the cell center, such as in Figs. 25(a), 27(a) and (b). In this case, the cold zones located at the negative tab and the bottom of the cell below positive tab (Fig. 27(a) and (b)), or sometimes located slightly left to the cell center (Fig. 25(a)).

(2) The hottest spot and its location shift

For all tests under adiabatic and natural convection conditions, the hottest spot (either inside or surface) of the cell located near the positive tab. This conclusion has been generally accepted since the current density near both tabs is always higher, and the material of positive tab (e.g. aluminum) is more advantageous on heat generation than the negative tab material (e.g. nickel-plating copper) due to the different electrical resistance of the two materials. However, not like the natural convection and adiabatic conditions, under the forced convection, the hottest spot was switched from the positive tab to the lower right of cell center at the later part of the discharge with lower rates (such as 0.3 C). The location shift of the hottest spot under forced convection might be attributed to the effective heat transfer through the tabs immersed in high-speed flowing air.

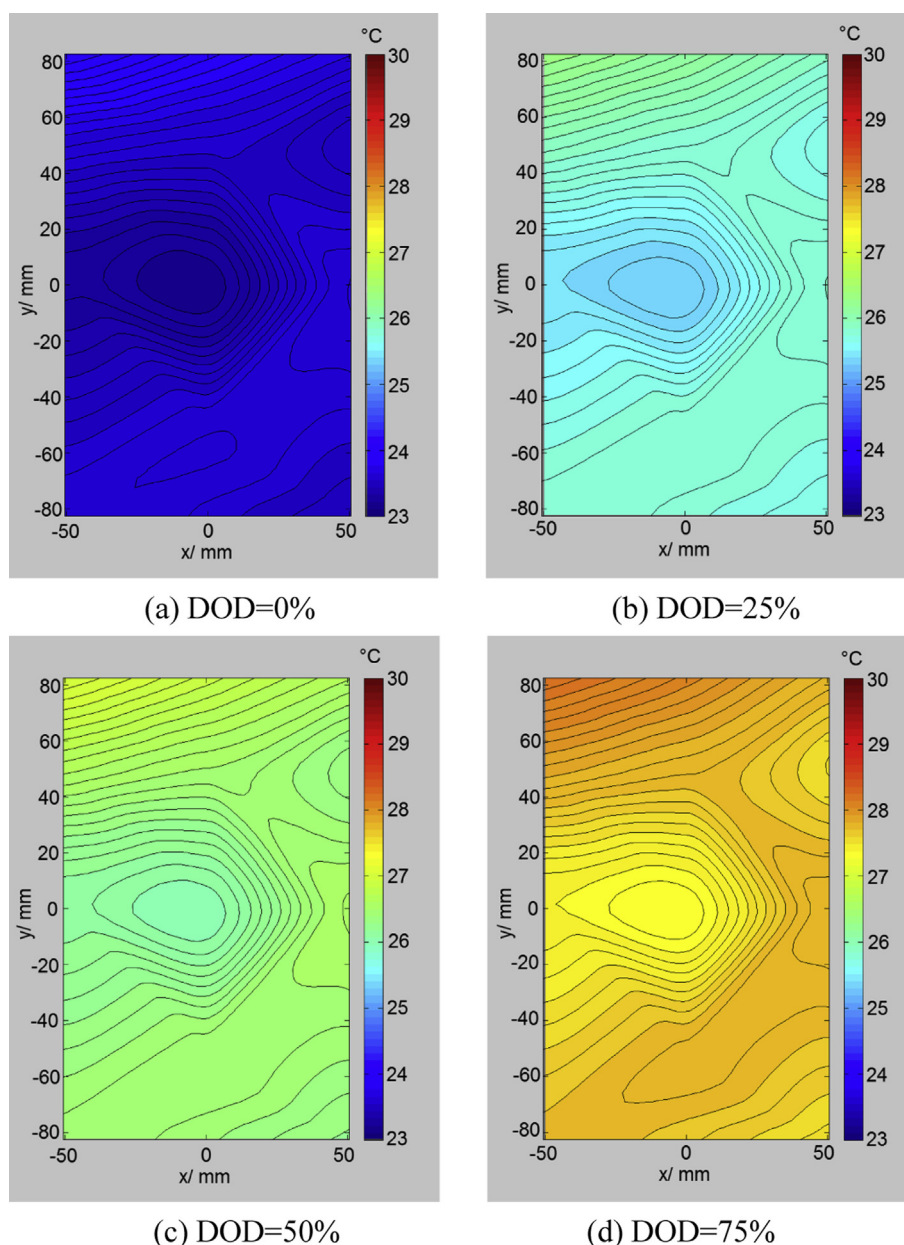


Fig. 28. The stable cold zone left to the cell center (internal temperature distribution during 0.3 C discharge under the adiabatic condition).

With the decrease of discharge rates, the heat dissipation through the tabs became more dominant than the heating-up effect on tabs and triggered the location shift of the hottest spot.

Here a comparable test result on the thermocouple-embedded 5 Ah cell was provided to further discuss this location shift. It was found that if larger discharge rates were applied (e.g. 2 C–5 C), even in the adiabatic tests, the temperature at the center of the 5 Ah cell finally surpassed the positive tab area at the end of discharge. Table 8 shows the DOD state when the temperature in the center overtook the positive tab area.

There are manifold causes for the hottest location shift of the 5 Ah cell in the adiabatic condition. Firstly, the adiabatic calorimeter kept tracking the cell temperature through the feedback-control of the heaters in the chamber to achieve adiabatic environment. The feedback sensor of cell temperature was arranged at a single point on cell surface. Since the local temperature of the positive tab area was generally hotter than at the feedback sensor in the early stages, even in the adiabatic calorimeter, the cell might actually dissipate heat to the calorimeter cavity through the tab, which slowed down the temperature rising of the tab area in the later part; Secondly, under larger discharge rates like 2 C–5 C, the reactants near the positive tab were severely depleted due to the initial higher temperature and faster electrochemical reaction. The center area with abundant reactants became more favorable for the following reactions, causing the location shift of the hottest spot finally [12,13].

(3) The shrinking of the cold zone

During the 0.3 C discharge under the adiabatic condition, there existed a stable cold zone slightly left to the cell center (Fig. 28). With the enlargement of discharge rates (e.g. 1.5 C), the cold zone was gradually squeezed in the early stages of discharge and shrank in size until it disappeared. The temperature distribution under 1.5 C adiabatic discharge is shown in Fig. 29 to show the shrinking process of the cold zone.

4.5. The temperature variation of the 12 internal locations

The temperature variation inside the cell will result in different thermal degradation at these internal locations, and existing degradation models [14–18] should be improved to take this factor into account. Consequently, the internal temperature variation should be considered in evaluating battery thermal design as an important indicator of battery inner nonuniformity. Fig. 30 shows the maximum temperature variation of 12 internal locations at the end of discharge.

It should be noted that the maximum temperature variation might not necessarily appear at the end of discharge, and Table 9 summarizes the cell DOD when the maximum variation was formed.

- (1) The temperature variation of internal locations could be considerably large, and the difference reached up to above 10 °C

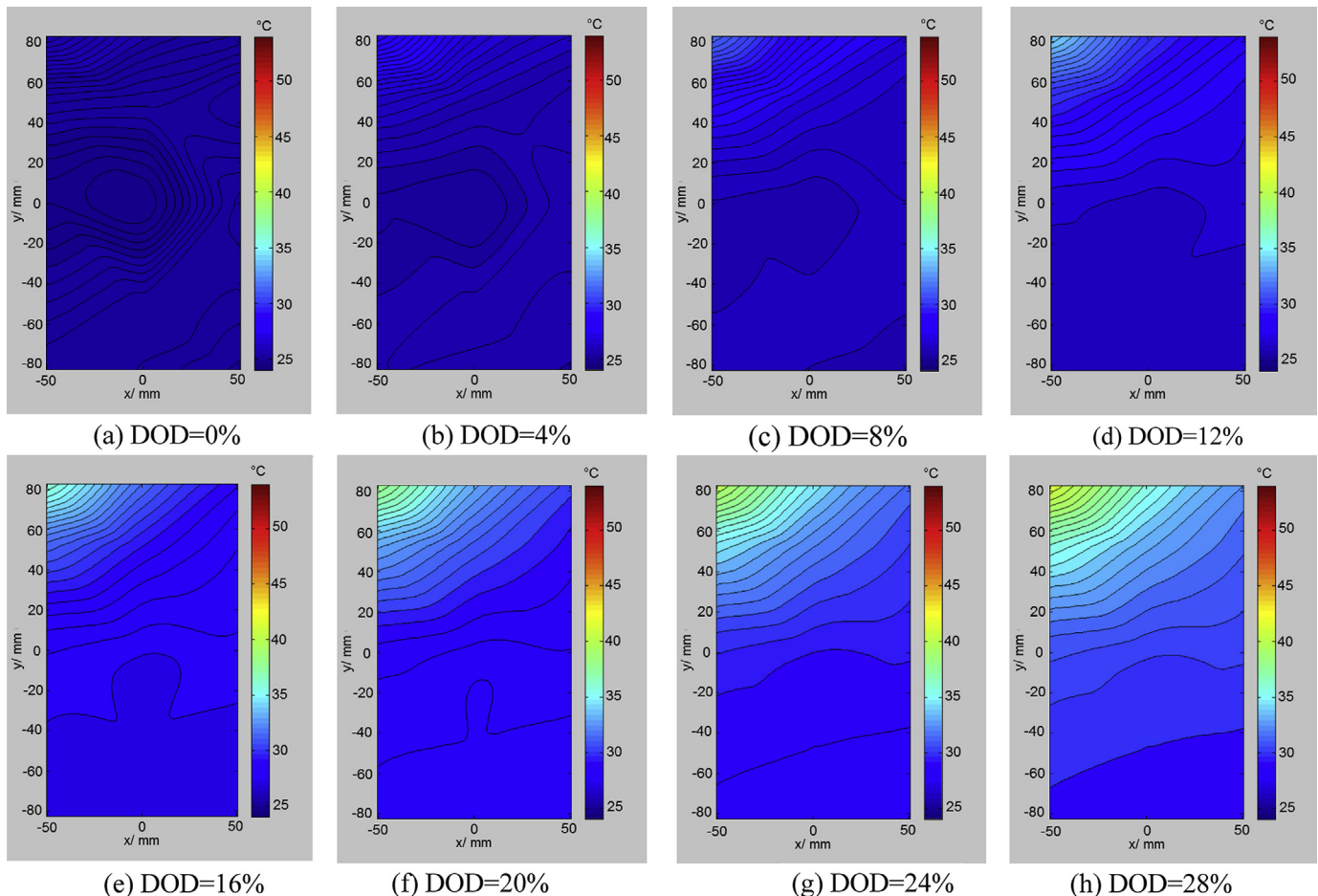


Fig. 29. The shrinking process of the cold zone left to the cell center (internal temperature distribution during 1.5 C discharge under the adiabatic condition).

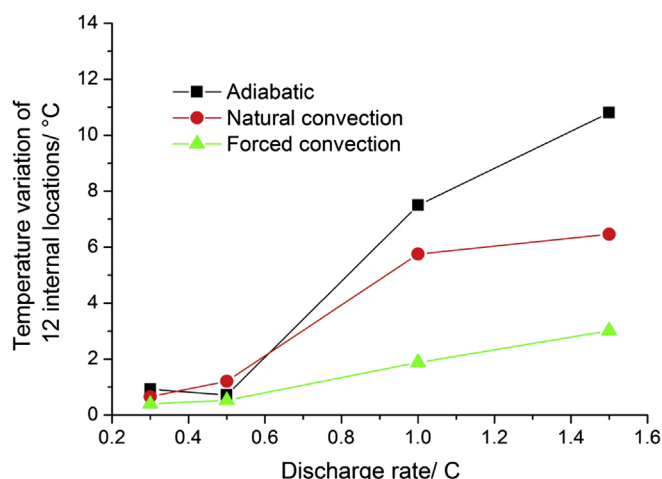


Fig. 30. The maximum temperature variation of 12 internal locations at the end of discharge.

Table 9

The timing of the maximum variation appearance (✓ = at the end of discharge, others in specific DOD).

Discharge rate	Adiabatic	Natural convection	Forced convection
0.3 C	DOD = 50%	DOD = 35%	✓
0.5 C	DOD = 50%	DOD = 35%	DOD = 55%
1 C	✓	✓	DOD = 50%
1.5 C	DOD = 50%	DOD = 50%	DOD = 50%

under 1.5 C discharge in the adiabatic calorimeter. (Due to the discrete locations of the thermocouples, it could be higher indeed). Thus, using one-point temperature to characterize the overall state of cell could be very risky. It might lead to the neglect of serious internal nonuniformity, and cause the overestimation of battery thermal safety under severe working cycles.

- (2) The correlation of internal temperature variation and discharge rates

For the same boundary conditions, the temperature nonuniformity inside the cell got stronger when the discharge rate increased. Temperature differences and discharge rates showed an approximate linear relationship in the rate range of these tests.

- (3) Sensitivity to boundary conditions

Increasing the convection heat transfer coefficient could significantly depress the development of internal temperature variation. The maximum internal variation had been decreased to less than 3 °C under the forced convection.

Therefore, for electric vehicle power systems, effective heat dissipation strategy should be considered for both suppressing the temperature rise and improving the inner uniformity. The actuator of the cooling system and its power capability should be carefully designed and calculated according to the battery thermal characteristic (as well as its evolution) obtained in lab experiments.

5. Conclusions and future work

The main conclusions of this paper are as follows:

- (1) The thermocouples embedded at multiple-points inside a laminated cell were found durable in months and capable of measuring battery internal temperature variations, indicating that the method we proposed was feasible and reliable.

- (2) Even if the tested cell has a thickness as thin as 7 mm, the internal temperature differed from the temperature at the corresponding locations on the surface for as large as 1.1 °C. The inside-and-surface temperature difference of a prismatic or cylindrical cell with the same capacity is expected to be even larger. Therefore, the temperature at a single point on the surface can not represent the overall thermal state of a large-format laminated cell. Measurement of internal temperature at multiple points inside large-format traction battery is essential to study the thermal property of the cell, as well as to validate the thermo-electrochemical models.
- (3) The thermal response of the cell when subjected to the step rise of the environmental temperature was examined. The response time constants at the internal and surface locations distributed in the range of 439 s–620 s. Compared with locations in the central area, the zones near peripheral region responded faster (having smaller time constants) on the temperature rise. The time constants of internal locations were generally larger than that at the locations on the surface, and the difference varied from 27 s to 70 s.
- (4) The temperature variation in the plane direction reached to as large as 10 °C under moderate discharge in adiabatic environment, which was much larger than that of through-plane direction. The thermal conductivity in the plane direction needs to be increased significantly for the tested cell.
- (5) Forced convection was found to be effective in suppressing both the rise and the variation of the temperature. Therefore, proper ventilation could be a viable option for the heat dissipation of the tested cell and should be actively explored in the BTMS.

The 25 Ah cell embedded with 12 thermocouples will be disassembled after the ongoing tests are completed, to find out the condition of the sensors as well as their impact on the battery material and structure. Since the thermocouple at the location A7 has failed during the cycles, the detailed analysis will be carried out on this thermocouple to investigate the failure mechanism.

The measured temporal and spatial variation of temperature is being used to validate the thermo-electrochemical models under development in our lab. Effort is also being made to probe other internal informations inside the cell, such as the distribution of potential and current density. Combined with the recently-published developments about the integrated micro temperature and voltage sensors [10], more inside informations both on battery thermal and electrical states, which are critical but previously-hidden, will be extracted.

Acknowledgment

This work is supported by the National Natural Science Foundation of China under the grant number of 20121302116, the National 863 Program under the subject number of 20121867607, and the Independent Research Programs of Tsinghua University under the subject number of 2011Z01004.

References

- [1] A.R. Mayyas, M. Omar, P. Pisu, et al., *Journal of Power Sources* 196 (15) (2011) 6588–6594.
- [2] R. Sabbah, R. Kizilel, J.R. Selman, et al., *Journal of Power Sources* 182 (2) (2008) 630–638.
- [3] R. Kizilel, A. Lateef, R. Sabbah, et al., *Journal of Power Sources* 183 (1) (2008) 370–375.
- [4] R. Mahamud, C. Park, *Journal of Power Sources* 196 (13) (2011) 5685–5696.
- [5] L. Jasinski, Rapid Battery Charging System and Method, U.S. Patent 3,852,652, Dec 3, 1974.
- [6] W.F. Fang, O.J. Kwon, C.Y. Wang, *International Journal of Energy Research* 34 (2) (2010) 107–115.

- [7] Y. Hu, S. Yurkovich, Y. Guezennec, et al., *Journal of Power Sources* 196 (1) (2011) 449–457.
- [8] Y.H. Ye, Y.X. Sh, N.S. Cai, et al., *Journal of Power Sources* 199 (1) (2012) 227–238.
- [9] C. Forgez, D.V. Do, G. Friedrich, et al., *Journal of Power Sources* 195 (9) (2010) 2961–2968.
- [10] C.Y. Lee, S.J. Lee, M.S. Tang, et al., *Sensors* 11 (2011) 9942–9950.
- [11] C.Y. Lee, F.B. Weng, C.K. Cheng, et al., *Journal of Power Sources* 205 (5) (2012) 345–349.
- [12] K.H. Kwon, C.B. Shin, T.H. Kang, et al., *Journal of Power Sources* 163 (1) (2006) 151–157.
- [13] G.X. Hu, J.Y. Xie, C.X. Li, et al., *Chinese Journal of Power Sources* 27 (s1) (2003) 201–204.
- [14] Z. Li, L.G. Lu, M.G. Ouyang, et al., *Journal of Power Sources* 196 (22) (2011) 9757–9766.
- [15] K. Takei, K. Kumai, Y. Kobayashi, *Journal of Power Sources* 97–98 (2001) 697–701.
- [16] I. Bloom, B.W. Cole, J.J. Sohn, et al., *Journal of Power Sources* 101 (2) (2001) 238–247.
- [17] Y.C. Zhang, C.Y. Wang, X.D. Tang, *Journal of Power Sources* 196 (3) (2011) 1513–1520.
- [18] J. Wang, P. Liu, J.H. Garner, et al., *Journal of Power Sources* 196 (8) (2011) 3942–3948.